

---

This manuscript has been submitted for publication in Nature Geoscience. Please note that the manuscript is not peer reviewed. Subsequent versions may have slightly different content.

If accepted, the final version will be available via the DOI link.

Please feel free to contact any of the authors.

---

1 Bridging spatiotemporal scales of fault growth during  
2 continental extension

3  
4 Sophie Pan<sup>1\*</sup>, John Naliboff<sup>2</sup>, Rebecca Bell<sup>1</sup> and Chris Jackson<sup>3</sup>

5 <sup>1</sup>Department of Earth Science and Engineering, Imperial College, Prince Consort Road, London, SW7  
6 2BP, UK

7 <sup>2</sup>Department of Earth and Environmental Science, New Mexico Institute of Mining and Technology, NM,  
8 USA

9 <sup>3</sup>Department of Earth and Environmental Sciences, The University of Manchester, Williamson Building,  
10 Oxford Road, Manchester, M13 9PL, UK

11 \*Corresponding author: Sophie Pan (sophie.pan16@imperial.ac.uk)

12

13 **Abstract**

14 Continental extension is accommodated by the development of kilometre-scale normal  
15 faults, which grow by accumulating metre-scale earthquake slip over millions of years.

16 Reconstructing the entire lifespan of a fault remains challenging due to a lack of observational

17 data with spatiotemporal scales that span the relatively short-term earthquake cycle, and the

18 longer-term paleoseismic record. Using 3D numerical simulations of continental extension and

19 novel fault extraction, we examine key factors controlling the growth of large faults over  $10^4$ - $10^6$

20 yrs. Modelled faults quantitatively show key geometric and kinematic similarities with natural

21 fault populations, with early faults (<100 kyrs from initiation) exhibiting scaling ratios consistent

22 with those characterising individual earthquake ruptures. While finite lengths are rapidly  
23 established (<100 kyrs), active deformation is transient, migrating both along- and across-strike.  
24 Competing stress interactions determine the active strain distribution, which oscillate locally  
25 between localised and distributed endmembers. Modelling suggests that far-field dynamic  
26 triggering can drive rupture propagation, producing recurring, large through-going slip. Our  
27 findings demonstrate that fault growth and the related occurrence of earthquakes is more  
28 complex than that currently inferred from observing displacement patterns on now-inactive  
29 structures, which only provide a spatial- and time-averaged picture of fault kinematics and  
30 related geohazard.

## 31 **Introduction**

32         Recent advancements in geodetic measurements allow for high-resolution surface  
33 observations of crustal deformation (e.g., Elliott et al., 2016). Seismological and geodetic data  
34 from a particular earthquake are inverted using modelled fault geometry to infer slip distribution  
35 and magnitude (e.g., Wilkinson et al., 2015; Walters et al., 2018). These data show that  
36 individual earthquake rupture patterns are variable and complex, with events typically temporally  
37 and spatially clustered (e.g., Coppersmith, 1989; Nicol et al., 2006). Rupture lengths are often  
38 considerably shorter than finite fault lengths, and multiple segment ruptures during a single event  
39 can trigger surprisingly high-magnitude, hazardous earthquakes (7.9  $M_w$  Kaikoura, New  
40 Zealand; Hamling et al., 2017; 7.2  $M_w$  El Mayor-Cucapah, Mexico; Fletcher et al., 2014) that  
41 have recently challenged seismic hazard assessments (Field et al., 2014).

42         Large (e.g., tens of kilometres long, several kilometres of displacement) normal faults  
43 grow by accumulating m-scale slip during earthquakes. In contrast to the short-time complexity

44 captured by seismological and geodetic data, 3D seismic reflection and field data show that slip  
45 rates can be stable over substantially longer timescales (i.e.,  $>10^6$  yrs), incorporating potentially  
46 thousands of seismic cycles distributed over millions of years. Using these data it is unclear  
47 whether fault displacement (i.e., cumulative slip) may simultaneously increase with length (the  
48 ‘propagating’ model; Walsh and Watterson, 1988), or if it accumulates on faults of near-constant  
49 length (the ‘constant-length’ model; Walsh et al., 2002). It is challenging to reconstruct fault  
50 growth over shorter timescales ( $< 10^6$  yrs) using these data, principally due to: (i) limited seismic  
51 reflection data resolution in the subsurface; (ii) the lack of exposures of hangingwall growth  
52 strata in the field; and (iii) a lack of age-constraints on syn-kinematic (growth) strata in both  
53 subsurface and field (Jackson et al., 2017).

54         Due to the lack of observational datasets of the appropriate temporal and spatial scale, it  
55 remains unclear how complex incremental slip patterns manifest and eventually result in stable,  
56 long-term displacement accumulation across large, mature faults. Slip rates measured from  
57 geodetic measurements such as Interferometric Synthetic Aperture Radar (InSAR) and Global  
58 Navigation Satellite System (GNSS) are often used to infer their geological rates (e.g., Wallace  
59 et al., 2009), but the former often appear systematically higher than the latter (Dixon et al., 2003;  
60 Oskin 2007; Bell et al., 2011). Bridging the spatiotemporal gaps, particularly over intermediate  
61 timescales ( $10^4$ - $10^6$  yrs), is therefore critical, given this can provide key first-order controls on  
62 slip geometry (Nicol et al., 2005, 2006), improving our ability to forecast the location and  
63 magnitude of potentially hazardous earthquakes (Roberts and Michetti, 2004).

64         Here, we use high-resolution ( $<650$  m) thermal-mechanical 3D simulations of continental  
65 extension to examine the evolution of normal fault networks across spatiotemporal scales poorly  
66 sampled by observational datasets. Using novel image processing techniques, the active length,

67 strain and cumulative strain are extracted from large fault populations across multiple timesteps  
68 and compared to natural D-L observations, providing insights into the kinematics that constrain  
69 fault growth, and the underlying dynamics that govern their evolution.

## 70 **Models produce realistic fault patterns**

71 Our model results show that in the final stages of rifting, the strain rate (Fig. 1a-c) and  
72 extracted active fault locations (Fig. 1d-f) for models with extension rates of 2.5, 5, or 10 mm yr<sup>-1</sup>  
73 reveal active deformation accommodated along complex fault networks. In models with faster  
74 extension rates, the overall magnitude of strain rate increases and is accommodated across  
75 increasingly diffuse zones of deformation (Fig. 1a-c). These networks contain faults of varying  
76 lengths (c. 5-120 km), which often contain along-strike changes in strike, and that may splay and  
77 link with adjacent structures. This complexity reflects both the randomisation of the initial plastic  
78 strain field and the mechanical and kinematic interaction between adjacent faults. Overall, the  
79 fault network is geometrically similar, based on displacement-length (D-L) scaling relationships,  
80 to those identified in natural systems (Fig. 2) (e.g., Walsh and Watterson, 1991; Kim and  
81 Sanderson, 2005).

## 82 **Fault patterns are rapidly established**

83 During the earliest stages of rifting, i.e., within the first resolvable timestep (c. 200, 100  
84 and 50 kyrs for extension rates of 2.5, 5, or 10 mm yr<sup>-1</sup>, respectively), active deformation is  
85 accommodated along distributed fault networks (Supplementary Video 1, 2) that are similar in  
86 appearance to their finite fault patterns (Fig. 1). During the earliest timestep (<100 kyrs) the  
87 faults are seemingly under-displaced compared to geological D-L datasets, instead plotting close

88 to the slip-length ratio associated with individual earthquakes ( $c = 0.00005$ ; see Wells and  
89 Coppersmith, 1994 and Fig. 2a).

90 As near-maximum finite fault lengths are established from the onset of extension, faults  
91 therefore predominantly accumulate displacement and move upwards in D-L space, behaviour  
92 consistent with the constant-length fault growth model (e.g., Walsh et al., 2002; Rotevatn et al.,  
93 2019; Pan et al., 2021). Our results show that fault lengths are established an order of magnitude  
94 (<100 kyrs) earlier than currently inferred from seismic reflection analysis of ancient (c. 1.3  
95 Myrs, NW Shelf, Australian; Walsh et al., 2002) and active (c. 700 kyrs, Whakatane Graben,  
96 New Zealand; Taylor et al., 2004) rifts. This rapid establishment of fault patterns suggest fault  
97 array growth is kinematically coherent (i.e., faults are part of a larger structure; Walsh and  
98 Watterson, 1991; Nicol et al., 2006) from the onset of extension. However, during early  
99 extension, all faults are blind and are not topography expressed at the model surface, therefore  
100 while lengths rapidly propagated laterally at depth, they may not have propagated vertically into  
101 the structural level of observation. This is important, given it is deformation of the Earth's  
102 surface, and resulting thickness and facies changes in associated growth strata, that are typically  
103 used to constrain normal fault kinematics (Jackson et al., 2017). The stratigraphic record may  
104 therefore not record the earliest phase of extension leading to an erroneous assessment of  
105 existing fault growth models and the timing of rift initiation and duration.

## 106 **Strain accumulation reveals transient behaviour**

107 Distinguishing between currently debated fault growth models has direct implications for  
108 the nature of earthquake slip and potential moment magnitude, i.e., the 'propagating' model is  
109 said to require a progressive temporal increase in the maximum earthquake magnitude, whereas

110 the constant-length model may be associated with constant slip rates and invariant earthquake  
111 magnitude and recurrence (Nicol et al., 2005). Whereas our results demonstrate that finite  
112 lengths were rapidly established (i.e., ‘constant-length’ model), they do not explicitly support  
113 either of the two slip models, instead showing that active deformation is temporally and spatially  
114 variable (i.e., earthquake slip is variable, not uniform), an observation consistent with slip  
115 patterns characterising active fault networks (e.g., Friedrich et al., 2003; Oskin et al., 2007) and  
116 analogue models (e.g., Schlagenhauf, 2008)

117 Time-series of the total number of active faults (Fig. 2b) and the average fault length in a  
118 given population (Fig. 2c) reveal significant fluctuations throughout time. All three models (with  
119 extensions rates of 2.5, 5, 10 mm yr<sup>-1</sup>) initiate with an increase in fault number and average fault  
120 length (Fig. 2b, c), corresponding to an initially diffuse distributed pattern from the first timestep  
121 that rapidly localises (i.e., reduces in deformation width) within the first c. 10 timesteps (see  
122 Supplementary Videos 1-2, 4-6). Both fault number and mean length continue to fluctuate  
123 throughout the remainder of extension, reflecting oscillations between localised and distributed  
124 active deformation throughout the crust (Fig. 2b, c). This behaviour is consistent with  
125 spatiotemporal clustering of earthquakes promoted by stress interactions between neighbouring  
126 faults (Stein 1999). Although transient behaviour continues for the remainder of extension, the  
127 overall number of faults slowly decreases, and the average fault length slightly increases (Fig.  
128 2b, c), demonstrating that large-scale localisation occurs as strain is concentrated onto fewer,  
129 larger fault systems (e.g., Cowie, 1998).

130 Transient deformation occurs both along- and perpendicular to strike, which we view in a  
131 regional model subset (Supplementary Video 4-6). Along-strike migration of deformation, which  
132 we observe by summing longitudinally across the regional subset (Supplementary Video 7), is

133 consistent with the preferential propagation direction of rupture. The across-strike strain  
134 migration correlates to along-strike bends, supporting observations from active settings that  
135 earthquakes occur at segment boundaries (DuRoss et al., 2016), and that relays may be  
136 associated with throw rate enhancements (Faure-Walker et al., 2009; Iezzi et al., 2018). Overall,  
137 both along- and across- strain migration, reflective of competing stress-interactions between  
138 faults in the near field (e.g., Cowie, 1998) as documented in Fig. 2b and c, produce end-member  
139 behaviours characterised by localised, continuous slip (Fig. 3a-c) and distributed, segmented slip  
140 (Fig. 3d-f). This transient behaviour evolves without explicitly modelling the earthquake cycle  
141 via a rate or rate-state friction type rheology (e.g., Dinther et al., 2013), suggesting that the  
142 recurrence of large, clustered slip (e.g., Fig. 3a) can be mechanically underpinned by far-field,  
143 dynamic triggering i.e., constant rates of tectonic extension. Faster extension rates ( $10 \text{ mm yr}^{-1}$ )  
144 result in more greater fluctuations between the aforementioned endmembers (Fig. 2b-c), resulting in  
145 sudden, large, recurring through-going slip events (Fig. 3),

146         The short-term variability and long-term stability of strain accumulation on the modelled  
147 fault networks may be reconciled by considering how deformation is aggregated, both spatially  
148 and temporally. As deformation is summed across (latitudinally) increasing regions, the strain  
149 rate profile along-strike becomes increasingly uniform as strain deficits in one location is  
150 compensated for by increased strain in other, across-strike locations (Supplementary Video 7).  
151 This reflects the coherence of faults at spatial scales larger than the individual fault surface (e.g.,  
152 Nicol et al., 2006). Small-scale, distributed deformation in the form of near-fault drag accounted  
153 for 30% greater geodetic slip rates (Oskin 2007). We suspect this value could be higher if the  
154 spatial scale of observation increases to accommodate all distributed deformation, particularly at  
155 higher extension rates ( $10 \text{ mm yr}^{-1}$ ) where distributed deformation is relatively widespread (e.g.,

156 Fig. 1). Furthermore, if geodetic rates are more likely to be measured from clustered earthquake  
157 slip (i.e., Fig. 3a-c), this may likely transiently exceed the geological slip average, given that  
158 interseismic periods of diffuse deformation (i.e., Fig. 3d-f) are less likely to be recorded, if  
159 deformation is expressed at all.

160 These findings demonstrate that fault network evolution is more complex than currently  
161 inferred from observing finite displacement patterns on now-inactive structures (i.e., finite strain  
162 in Fig. 3b and 3e appear nearly identical), which provide only a time-averaged picture of fault  
163 kinematics. Subsequently, geodetic rates will not necessarily mirror geological rates, as it may  
164 only capture a transient snapshot. Conventional D-L profiles may therefore provide only a  
165 limited understanding of fault growth, given they do not capture stress- and -time dependent  
166 stress interactions crucial to revealing the short- to intermediate-timescale variations in faulting  
167 that control earthquake magnitude and location.

## 168 **Methods**

### 169 **Model Geometry and Resolution**

170 The governing equations are solved on a 3D gridded domain which spans 500 by 500 km  
171 across the horizontal plane (X, Y) and 100 km in the depth (Z) direction. The grids are coarsest  
172 (5 km) on the sides and base of the model domain and are successively reduced using adaptive-  
173 mesh refinement, increasing the resolution to 625 m over a centered 180 x 180 x 20 km region  
174 (Supplementary Fig. 1). Broadly, this approach provides ‘natural’ boundary conditions for  
175 distributed fault networks within the upper crust.

### 176 **Governing equations**

177 We use the open-source, mantle convection and lithospheric dynamics code ASPECT  
 178 (Kronbichler et al., 2012; Heister et al., 2017) to model 3D continental extension following the  
 179 approach of Naliboff et al. (2020). The model solves the incompressible Boussinesq  
 180 approximation of momentum, mass and energy equations, combined with advection-diffusion  
 181 equations which are outlined below. The Stokes equation which solves for velocity and pressure  
 182 are defined as:

$$183 \quad \nabla \cdot \mathbf{u} = 0 \quad (1)$$

$$184 \quad -\nabla \cdot 2 \mu \dot{\epsilon}(\mathbf{u}) + \nabla p = \rho \mathbf{g} \quad (2)$$

185 Where  $\mathbf{u}$  is the velocity,  $\mu$  is the viscosity,  $\dot{\epsilon}$  is the second deviator of the strain rate tensor,  $p$  is  
 186 pressure,  $\rho$  is density, and  $\mathbf{g}$  is gravitational acceleration.

187 Temperature evolves through a combination of advection, heat conduction, shear heating,  
 188 and adiabatic heating:

$$189 \quad \rho C_p \left( \frac{\partial T}{\partial t} + \mathbf{u} \cdot \nabla T \right) - \nabla \cdot (\kappa \rho C_p) \nabla T = \rho H + 2\eta \dot{\epsilon}(\mathbf{u}) + \alpha T (\mathbf{u} \cdot \nabla p) \quad (3)$$

190 Where  $C_p$  is the heat capacity,  $T$  is temperature,  $t$  is time,  $\kappa$  is thermal diffusivity, and  $H$  is the  
 191 rate of internal heating. Respectively, the terms on the right-hand side correspond to internal  
 192 head production, shear heating, and adiabatic heating.

193 Density varies linearly as a function of the reference density ( $\rho_0$ ), thermal expansivity  
 194 ( $\alpha$ ), reference temperature ( $T_0$ ) and temperature:

$$195 \quad \rho = \rho_0 (1 - \alpha (T - T_0)) \quad (4)$$

## 196 **Rheological Formulation**

197 Rheological behaviour combines nonlinear viscous flow with brittle failure (see Glerum  
198 et al., 2018). Viscous flow follows dislocation creep, formulated as:

$$199 \quad \sigma'_{II} = A \frac{1}{n} \dot{\epsilon}'_{II} \frac{1}{n} e^{\frac{Q+PV}{nRT}} \quad (5)$$

200 Above,  $\sigma'_{II}$  is the second invariant of the deviatoric stress,  $A$  is the viscous prefactor,  $n$  is the  
201 stress exponent,  $\dot{\epsilon}'_{II}$  is the second invariant of the deviatoric strain rate (effective strain rate),  $Q$  is  
202 the activation energy,  $P$  is pressure,  $V$  is the activation volume,  $T$  is temperature, and  $R$  is the gas  
203 constant

204 Brittle plastic deformation follows a Drucker Prager yield criterion, which accounts for  
205 softening of the angle of internal friction ( $\phi$ ) and cohesion ( $C$ ) as a function of accumulated  
206 plastic strain:

$$207 \quad \sigma'_{II} = \frac{6 C \cos \phi + 2 P \sin \phi}{\sqrt{(3)(3 + \sin \phi)}} \quad (6)$$

208 The initial friction angle and cohesion are 30 and 20 MPa respectively, and linearly weaken by a  
209 factor of 2 as a function of finite plastic strain. Rather than a single weak seed (e.g., Lavier et al.,  
210 2000; Huisman et al., 2007), or randomised distribution (e.g., Naliboff et al., 2020; Duclaux et  
211 al., 2020), we localise deformation by partitioning initial plastic strain into 5 km coarse blocks  
212 which are randomly assigned 0.5 or 1.5. This results in statistically random but pervasive  
213 damage using an adjustable wavelength (i.e., the block size). From a geological perspective, the  
214 initial strain field here may reflect structural inheritance observed in natural systems, where  
215 deformation exploits inherited weaknesses such as pre-existing faults (e.g., Phillips et al., 2016)  
216 or the margins of strong zones (e.g., ancient cratons; e.g., Dunbar and Sawyer, 1989).

217           The viscosity is calculated using the viscosity rescaling method, where if the viscous  
218 stress exceeds plastic yield stress, the viscosity is reduced such that the effective stress matches  
219 the plastic yield (see Glerum et al., 2018). Nonlinearities from the Stokes equations are  
220 addressed by applying defect-Picard iterations (Fraters et al., 2019) to a tolerance of  $1e^{-4}$ . The  
221 maximum numerical time step is limited to 20 kyrs.

## 222 **Initial Conditions**

223           The model domain contains three distinct compositional layers, representing the upper  
224 crust (0-20 km depth), lower crust (20-40 km depth), and lithospheric mantle (40-100 km depth).  
225 Distinct background densities (2700, 2800, 3300  $\text{kg m}^{-3}$ ) and viscous flow laws for dislocation  
226 creep (wet quartzite (Gleason and Tullis, 1995), wet anorthite (Rybacki et al., 2003), dry olive  
227 (Hirth and Kohlstedt, 2003) distinguish these three layers, which deform through a combination  
228 of nonlinear viscous flow and brittle (plastic) deformation (Glerum et al., 2018; Naliboff et al.,  
229 2020). Supplementary Table 1 contains the specific parameters for each flow law.

230           The initial temperature distribution follows a characteristic conductive geotherm for the  
231 continental lithosphere (Chapman, 1986). We solve for the conductive profile by first assuming a  
232 thermal conductivity of  $2.5 \text{ W m}^{-1} \text{ K}^{-1}$ , a surface temperature of 273 K, and a surface heat flow of  
233  $55 \text{ mW/m}^2$ , and constant radiogenic heating in each compositional layer (Supplementary Table  
234 1) which we use to calculate the temperature with depth within each layer. The resulting  
235 temperature at the base of the upper crust, lower crust, and mantle lithosphere, respectively, are  
236 633, 893, and 1613 °K.

## 237 **Boundary Conditions**

238 Deformation is driven by prescribed outflow velocities on the left and right sides (i.e.,  
239 orthogonal extension), with inflow at the model base exactly balancing the outflow. The top of  
240 the model is a free surface (Rose et al., 2015) and is advected normal to the velocity field. The  
241 extension rate (i.e., the prescribed outward velocity) is 2.5, 5 and 10 mm yr<sup>-1</sup> (Fig. 1).

## 242 **Fault extraction workflow**

243 The 3D model results are analysed on a horizontal plane located 5 km below the initial  
244 model surface. To quantitatively analyse the geometry and kinematics of faults, fault  
245 identification and extraction is required. The input image can be a depth slice of any field  
246 documenting strain - our results use  $\frac{\partial v_z}{\partial x}$  as this reveals the dip direction of active faults  
247 (Supplementary Fig. 2a). The input slice is derived with respect to depth and histogram  
248 equalisation is applied (Supplementary Fig. 2b) in order to i) allow for areas of lower contrast  
249 (i.e., smaller faults) to gain a higher contrast, enabling a comprehensive extraction of the entire  
250 fault population; and ii) globally adjust contrast for comparison across multiple timesteps. In  
251 effect, this step in the workflow produces a value of 0 on one side of the fault, and a value of 1  
252 on the other side of the fault (Supplementary Fig. 2b), such that in the presence of bifurcation,  
253 fault segments are separated.

254 The localities of fault segments are revealed by computing the difference between large  
255 contrasts along the longitudinal direction (Supplementary Fig. 2c), and a predetermined fraction  
256 of this range is used to threshold the image (Supplementary Fig. 2d). Here, this approach extracts  
257 localised, clustered regions of strain (i.e., relatively steep gradients of strain-profiles).

258 The binary array is labelled according to neighbouring connectivity of pixels  
259 (Supplementary Fig. 2e) (e.g., Dillencourt et al., 1992). Noise is filtered out by removing

260 labelled pixels which are smaller than 20. In the case that branching remains, a post-processing  
261 script breaks up any remaining branches by locating euclidean distance transformation anomalies  
262 which arise as a result of bifurcation, and use the locality as a mask to split labels into two  
263 discrete fault segments. As a result, this approach successfully recovers detailed interactions  
264 between distinct active fault strands without manual input across multiple timesteps  
265 (Supplementary Fig. 2f).

### 266 **Data availability**

267 The model output (including vtk data and log files) are provided with this paper. The parameter  
268 file and additional inputs used to run the models are also included. Models were run with  
269 ASPECT 2.2.0-pre on 720 processors (15 nodes). This version of ASPECT can be obtained with  
270 git checkout ab5eead39 from the main branch.

### 271 **Code availability**

272 The Python code used to extract faults will be made available through an open data repository.  
273 Python code used to generate the initial plastic strain, and the initial geothermal profile are  
274 included as a supplementary file.

### 275 **Acknowledgements**

276 PhD work is funded by Natural Environment Research Council (NERC) Centre for Doctoral  
277 Training (CDT) in Oil and Gas (NE/R01051X/1). The computational time for these simulations  
278 was provided under XSEDE project EAR180001.

279

280 **References**

- 281 1. Bell, R.E., McNeill, L.C., Henstock, T.J. and Bull, J.M., 2011. Comparing extension on  
282 multiple time and depth scales in the Corinth Rift, Central Greece. *Geophysical Journal*  
283 *International*, 186(2), pp.463-470.
- 284 2. Chapman, D.S., 1986. Thermal gradients in the continental crust. *Geological Society,*  
285 *London, Special Publications*, 24(1), pp.63-70.
- 286 3. Coppersmith, K.J. and Youngs, R.R., 1989. Issues regarding earthquake source  
287 characterization and seismic hazard analysis within passive margins and stable continental  
288 interiors. In *Earthquakes at North-Atlantic Passive Margins: Neotectonics and Postglacial*  
289 *Rebound* (pp. 601-631). Springer, Dordrecht.
- 290 4. Cowie, P.A., 1998. A healing–reloading feedback control on the growth rate of seismogenic  
291 faults. *Journal of Structural Geology*, 20(8), pp.1075-1087.
- 292 5. Dawers, N.H. and Underhill, J.R., 2000. The role of fault interaction and linkage in  
293 controlling synrift stratigraphic sequences: Late Jurassic, Statfjord East area, northern North  
294 Sea. *AAPG bulletin*, 84(1), pp.45-64.
- 295 6. Dillencourt, M.B., Samet, H. and Tamminen, M., 1992. A general approach to connected-  
296 component labeling for arbitrary image representations. *Journal of the ACM (JACM)*, 39(2),  
297 pp.253-280.
- 298 7. Dixon, T.H., Norabuena, E. and Hotaling, L., 2003. Paleoseismology and Global Positioning  
299 System: Earthquake-cycle effects and geodetic versus geologic fault slip rates in the Eastern  
300 California shear zone. *Geology*, 31(1), pp.55-58.

- 301 8. Duclaux, G., Huismans, R.S. and May, D.A., 2020. Rotation, narrowing, and preferential  
302 reactivation of brittle structures during oblique rifting. *Earth and Planetary Science*  
303 *Letters*, 531, p.115952.
- 304 9. Dunbar, J.A. and Sawyer, D.S., 1989. How preexisting weaknesses control the style of  
305 continental breakup. *Journal of Geophysical Research: Solid Earth*, 94(B6), pp.7278-7292.
- 306 10. DuRoss, C.B., Personius, S.F., Crone, A.J., Olig, S.S., Hylland, M.D., Lund, W.R. and  
307 Schwartz, D.P., 2016. Fault segmentation: New concepts from the Wasatch fault zone, Utah,  
308 USA. *Journal of Geophysical Research: Solid Earth*, 121(2), pp.1131-1157.
- 309 11. Elliott, J.R., Walters, R.J. and Wright, T.J., 2016. The role of space-based observation in  
310 understanding and responding to active tectonics and earthquakes. *Nature*  
311 *communications*, 7(1), pp.1-16.
- 312 12. Field, E.H., Arrowsmith, R.J., Biasi, G.P., Bird, P., Dawson, T.E., Felzer, K.R., Jackson,  
313 D.D., Johnson, K.M., Jordan, T.H., Madden, C. and Michael, A.J., 2014. Uniform California  
314 earthquake rupture forecast, version 3 (UCERF3)—The time-independent model. *Bulletin of*  
315 *the Seismological Society of America*, 104(3), pp.1122-1180.
- 316 13. Fletcher, J.M., Teran, O.J., Rockwell, T.K., Oskin, M.E., Hudnut, K.W., Mueller, K.J., Spelz,  
317 R.M., Akciz, S.O., Masana, E., Faneros, G. and Fielding, E.J., 2014. Assembly of a large  
318 earthquake from a complex fault system: Surface rupture kinematics of the 4 April 2010 El  
319 Mayor–Cucapah (Mexico) Mw 7.2 earthquake. *Geosphere*, 10(4), pp.797-827.
- 320 14. Fraters, M.R., Bangerth, W., Thieulot, C., Glerum, A.C. and Spakman, W., 2019. Efficient  
321 and practical Newton solvers for non-linear Stokes systems in geodynamic  
322 problems. *Geophysical Journal International*, 218(2), pp.873-894.

- 323 15. Friedrich, A.M., Wernicke, B.P., Niemi, N.A., Bennett, R.A. and Davis, J.L., 2003.  
324 Comparison of geodetic and geologic data from the Wasatch region, Utah, and implications  
325 for the spectral character of Earth deformation at periods of 10 to 10 million years. *Journal of*  
326 *Geophysical Research: Solid Earth*, 108(B4).
- 327 16. Gleason, G.C. and Tullis, J., 1995. A flow law for dislocation creep of quartz aggregates  
328 determined with the molten salt cell. *Tectonophysics*, 247(1-4), pp.1-23.
- 329 17. Glerum, A., Thieulot, C., Fraters, M., Blom, C. and Spakman, W., 2018. Nonlinear  
330 viscoplasticity in ASPECT: benchmarking and applications to subduction. *Solid Earth*, 9(2),  
331 pp.267-294.
- 332 18. Hamling, I.J., Hreinsdóttir, S., Clark, K., Elliott, J., Liang, C., Fielding, E., Litchfield, N.,  
333 Villamor, P., Wallace, L., Wright, T.J. and D’Anastasio, E., 2017. Complex multifault  
334 rupture during the 2016 Mw 7.8 Kaikōura earthquake, New Zealand. *Science*, 356(6334).
- 335 19. Heister, T., Dannberg, J., Gassmüller, R. and Bangerth, W., 2017. High accuracy mantle  
336 convection simulation through modern numerical methods—II: realistic models and  
337 problems. *Geophysical Journal International*, 210(2), pp.833-851.
- 338 20. Hirth, G. and Kohlstedt, D., 2003. Rheology of the upper mantle and the mantle wedge: A  
339 view from the experimentalists. *Geophysical Monograph-American Geophysical Union*, 138,  
340 pp.83-106.
- 341 21. Huisman, R.S. and Beaumont, C., 2007. Roles of lithospheric strain softening and  
342 heterogeneity in determining the geometry of rifts and continental margins. *Geological*  
343 *Society, London, Special Publications*, 282(1), pp.111-138.
- 344 22. Iezzi, F., Mildon, Z., Walker, J.F., Roberts, G., Goodall, H., Wilkinson, M. and Robertson, J.,  
345 2018. Coseismic throw variation across along-strike bends on active normal faults:

- 346 Implications for displacement versus length scaling of earthquake ruptures. *Journal of*  
347 *Geophysical Research: Solid Earth*, 123(11), pp.9817-9841.
- 348 23. Jackson, C.A.L., Bell, R.E., Rotevatn, A. and Tvedt, A.B., 2017. Techniques to determine the  
349 kinematics of synsedimentary normal faults and implications for fault growth  
350 models. *Geological Society, London, Special Publications*, 439(1), pp.187-217.
- 351 24. Kim, Y.S. and Sanderson, D.J., 2005. The relationship between displacement and length of  
352 faults: a review. *Earth-Science Reviews*, 68(3-4), pp.317-334
- 353 25. Kronbichler, M., Heister, T. and Bangerth, W., 2012. High accuracy mantle convection  
354 simulation through modern numerical methods. *Geophysical Journal International*, 191(1),  
355 pp.12-29.
- 356 26. Lavier, L.L., Buck, W.R. and Poliakov, A.N., 2000. Factors controlling normal fault offset in  
357 an ideal brittle layer. *Journal of Geophysical Research: Solid Earth*, 105(B10), pp.23431-  
358 23442.
- 359 27. Naliboff, J.B., Glerum, A., Brune, S., Péron-Pinvidic, G. and Wrona, T., 2020. Development  
360 of 3-D rift heterogeneity through fault network evolution. *Geophysical Research*  
361 *Letters*, 47(13), p.e2019GL086611.
- 362 28. Nicol, A., Walsh, J., Berryman, K. and Villamor, P., 2006. Interdependence of fault  
363 displacement rates and paleoearthquakes in an active rift. *Geology*, 34(10), pp.865-868.
- 364 29. Nicol, A., Walsh, J.J., Manzocchi, T. and Morewood, N., 2005. Displacement rates and  
365 average earthquake recurrence intervals on normal faults. *Journal of Structural*  
366 *Geology*, 27(3), pp.541-551.

- 367 30. Oskin, M., Perg, L., Blumentritt, D., Mukhopadhyay, S. and Iriondo, A., 2007. Slip rate of  
368 the Calico fault: Implications for geologic versus geodetic rate discrepancy in the Eastern  
369 California Shear Zone. *Journal of Geophysical Research: Solid Earth*, 112(B3).
- 370 31. Phillips, T.B., Jackson, C.A., Bell, R.E., Duffy, O.B. and Fossen, H., 2016. Reactivation of  
371 intrabasement structures during rifting: A case study from offshore southern  
372 Norway. *Journal of Structural Geology*, 91, pp.54-73.
- 373 32. Roberts, G.P. and Michetti, A.M., 2004. Spatial and temporal variations in growth rates  
374 along active normal fault systems: an example from The Lazio–Abruzzo Apennines, central  
375 Italy. *Journal of Structural Geology*, 26(2), pp.339-376.
- 376 33. Roberts, G.P. and Michetti, A.M., 2004. Spatial and temporal variations in growth rates  
377 along active normal fault systems: an example from The Lazio–Abruzzo Apennines, central  
378 Italy. *Journal of Structural Geology*, 26(2), pp.339-376.
- 379 34. Rose, I., Buffett, B. and Heister, T., 2017. Stability and accuracy of free surface time  
380 integration in viscous flows. *Physics of the Earth and Planetary Interiors*, 262, pp.90-100.
- 381 35. Rotevatn, A., Jackson, C.A.L., Tvedt, A.B., Bell, R.E. and Blækkan, I., 2019. How do  
382 normal faults grow?. *Journal of Structural Geology*, 125, pp.174-184.
- 383 36. Rybacki, E., Gottschalk, M., Wirth, R. and Dresen, G., 2006. Influence of water fugacity and  
384 activation volume on the flow properties of fine-grained anorthite aggregates. *Journal of*  
385 *Geophysical Research: Solid Earth*, 111(B3).
- 386 37. Schlagenhauf, A., Manighetti, I., Malavieille, J. and Dominguez, S., 2008. Incremental  
387 growth of normal faults: Insights from a laser-equipped analog experiment. *Earth and*  
388 *Planetary Science Letters*, 273(3-4), pp.299-311.

- 389 38. Stein, R.S., 1999. The role of stress transfer in earthquake occurrence. *Nature*, 402(6762),  
390 pp.605-609.
- 391 39. Taylor, S.K., Bull, J.M., Lamarche, G. and Barnes, P.M., 2004. Normal fault growth and  
392 linkage in the Whakatane Graben, New Zealand, during the last 1.3 Myr. *Journal of*  
393 *Geophysical Research: Solid Earth*, 109(B2)
- 394 40. Thieulot, C., 2011. FANTOM: Two-and three-dimensional numerical modelling of creeping  
395 flows for the solution of geological problems. *Physics of the Earth and Planetary*  
396 *Interiors*, 188(1-2), pp.47-68.
- 397 41. Van Dinther, Y., Gerya, T.V., Dalguer, L.A., Corbi, F., Funicello, F. and Mai, P.M., 2013.  
398 The seismic cycle at subduction thrusts: 2. Dynamic implications of geodynamic simulations  
399 validated with laboratory models. *Journal of Geophysical Research: Solid Earth*, 118(4),  
400 pp.1502-1525.
- 401 42. Walker, J.F., Roberts, G.P., Cowie, P.A., Papanikolaou, I.D., Sammonds, P.R., Michetti,  
402 A.M. and Phillips, R.J., 2009. Horizontal strain-rates and throw-rates across breached relay  
403 zones, central Italy: Implications for the preservation of throw deficits at points of normal  
404 fault linkage. *Journal of Structural Geology*, 31(10), pp.1145-1160.
- 405 43. Wallace, L.M., Ellis, S., Miyao, K., Miura, S., Beavan, J. and Goto, J., 2009. Enigmatic,  
406 highly active left-lateral shear zone in southwest Japan explained by aseismic ridge  
407 collision. *Geology*, 37(2), pp.143-146.
- 408 44. Walsh, J.J. and Watterson, J., 1988. Analysis of the relationship between displacements and  
409 dimensions of faults. *Journal of Structural geology*, 10(3), pp.239-247.

- 410 45. Walsh, J.J., Nicol, A. and Childs, C., 2002. An alternative model for the growth of  
411 faults. *Journal of Structural Geology*, 24(11), pp.1669-1675.
- 412 46. Walters, R.J., Gregory, L.C., Wedmore, L.N., Craig, T.J., McCaffrey, K., Wilkinson, M.,  
413 Chen, J., Li, Z., Elliott, J.R., Goodall, H. and Iezzi, F., 2018. Dual control of fault  
414 intersections on stop-start rupture in the 2016 Central Italy seismic sequence. *Earth and  
415 Planetary Science Letters*, 500, pp.1-14.
- 416 47. Wells, D.L. and Coppersmith, K.J., 1994. New empirical relationships among magnitude,  
417 rupture length, rupture width, rupture area, and surface displacement. *Bulletin of the  
418 seismological Society of America*, 84(4), pp.974-1002.
- 419 48. Wilkinson, M., Roberts, G.P., McCaffrey, K., Cowie, P.A., Walker, J.P.F., Papanikolaou, I.,  
420 Phillips, R.J., Michetti, A.M., Vittori, E., Gregory, L. and Wedmore, L., 2015. Slip  
421 distributions on active normal faults measured from LiDAR and field mapping of  
422 geomorphic offsets: an example from L'Aquila, Italy, and implications for modelling seismic  
423 moment release. *Geomorphology*, 237, pp.130-141.

## 424 **Figure captions**

425 **Figure 1.** The top row shows the strain rate invariant ( $s^{-1}$ ) in the upper crust (extracted at 5 km  
426 depth), documenting active deformation patterns within the last resolvable time increment for  
427 models ran at 2.5, 5, and 10 mm yr<sup>-1</sup> respectively. The bottom row shows their corresponding  
428 fault length extracted from the active deformation field. See Supplementary Video 2 for  
429 animation across all modelled timesteps.

430

431 **Figure 2.** Geometric statistics of time-dependent fault properties. **a)** Fault D-L evolution for the  
432 modelled fault network that experienced  $5 \text{ mm yr}^{-1}$  extension. Observational datasets are plotted  
433 in grey, where different shades correlate to references therein. See Supplementary Video 3 for  
434 animation across all models. **b)** The number of active faults throughout time. **c)** The average  
435 active length of the network throughout time. Note that all three models output 50 timesteps,  
436 however the total extension duration for models deformed at  $2.5$ ,  $5$  and  $10 \text{ mm yr}^{-1}$  are 10, 5 and  
437 2.5 Myrs, respectively.

438

439 **Figure 3.** End-member behaviour of transient deformation. Along-strike maps from a subset of  
440 the model that experienced  $10 \text{ mm yr}^{-1}$  extension. The strain rate invariant **(a)**, finite strain **(b)**,  
441 and extracted faults **(c)** at 2.1 Myrs reveal localised, continuous behaviour. The strain rate **(d)**,  
442 finite strain **(e)** and extracted faults **(f)** at 2.2 Myrs reveal distributed, segmented behaviour.

**Figure 1.** The top row shows the strain rate invariant ( $s^{-1}$ ) in the upper crust (extracted at 5 km depth), documenting active deformation patterns within the last resolvable time increment for models ran at 2.5, 5, and 10 mm  $yr^{-1}$  respectively. The bottom row shows their corresponding fault length extracted from the active deformation field. See Supplementary Video 2 for animation across all modelled timesteps.

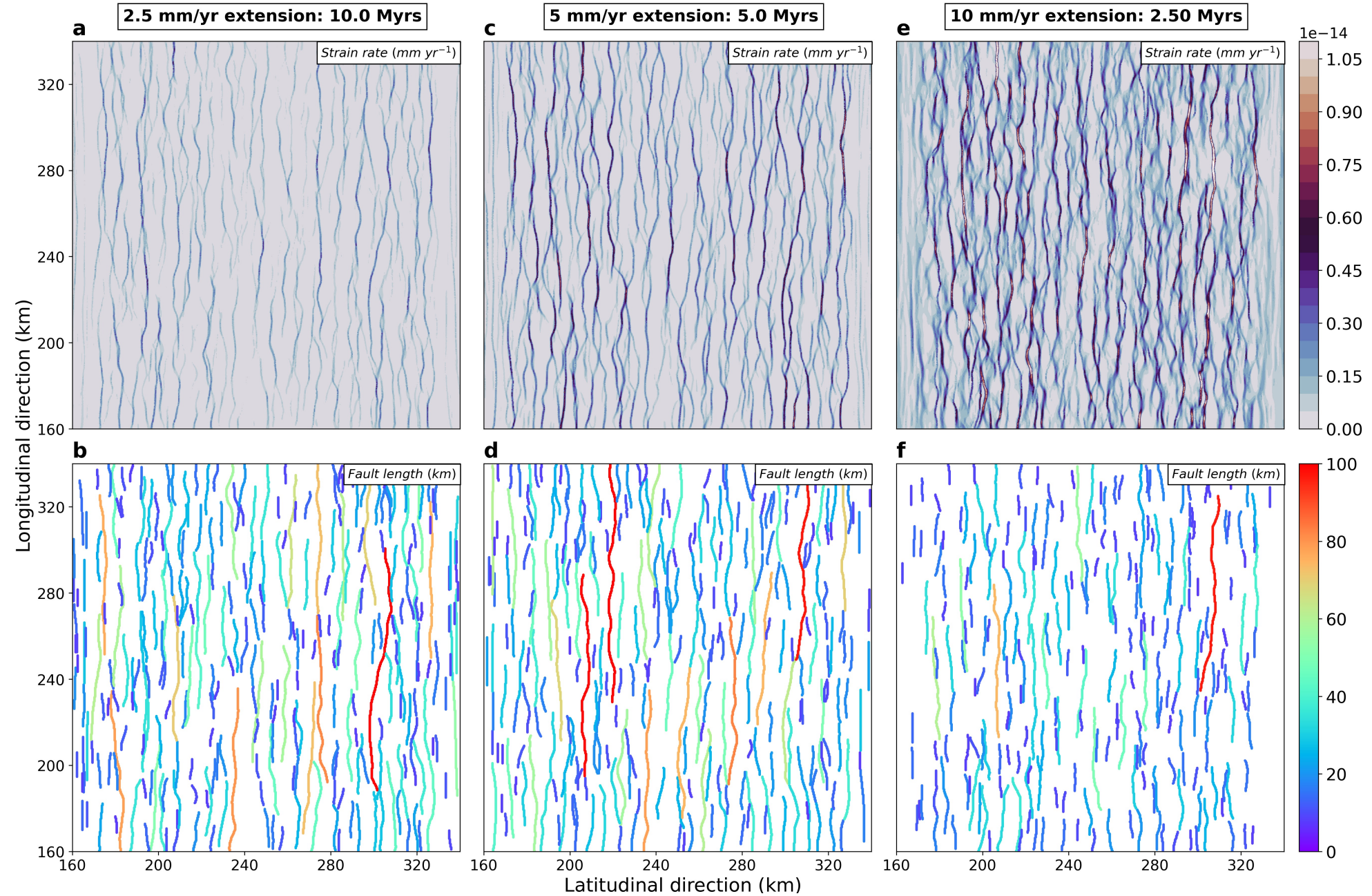


**Figure 2.** Geometric statistics of time-dependent fault properties. **a)** Fault D-L evolution for the modelled fault network that experienced  $5 \text{ mm yr}^{-1}$  extension. Observational datasets are plotted in grey, where different shades correlate to references therein. See Supplementary Video 3 for animation across all models. **b)** The number of active faults throughout time. **c)** The average active length of the network throughout time. Note that all three models output 50 timesteps, however the total extension duration for models deformed at  $2.5$ ,  $5$  and  $10 \text{ mm yr}^{-1}$  are  $10$ ,  $5$  and  $2.5 \text{ Myrs}$ , respectively.

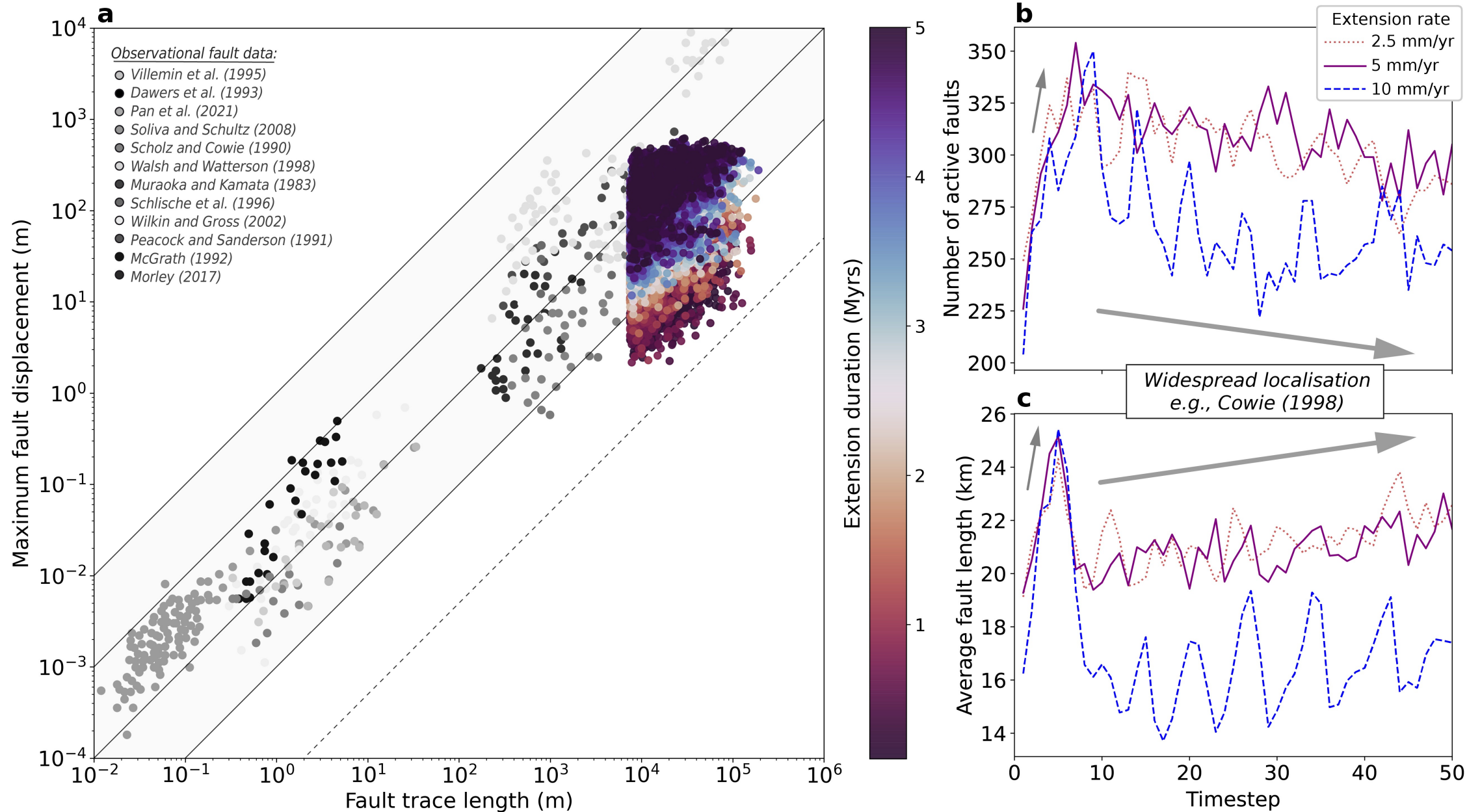


**Figure 3.** End-member behaviour of transient deformation. Along-strike maps from a subset of the model that experienced  $10 \text{ mm yr}^{-1}$  extension. The strain rate invariant **(a)**, finite strain **(b)**, and extracted faults **(c)** at 2.1 Myrs reveal localised, continuous behaviour. The strain rate **(d)**, finite strain **(e)** and extracted faults **(f)** at 2.2 Myrs reveal distributed, segmented behaviour.

